Nonlinear Dyn (2013) 73:689–704
DOI 10.1007/s11071-013-0823-x

ORIGINAL PAPER

# Detecting invariant manifolds, attractors, and generalized KAM tori in aperiodically forced mechanical systems

**Alireza Hadjighasem · Mohammad Farazmand · George Haller**

Received: 26 October 2012 / Accepted: 27 January 2013 / Published online: 22 February 2013


**Abstract** We show how the recently developed theory of geodesic transport barriers for fluid flows can be used to uncover key invariant manifolds in externally forced, one-degree-of-freedom mechanical systems. Specifically, invariant sets in such systems turn out to be shadowed by least-stretching geodesics of the Cauchy–Green strain tensor computed from the flow map of the forced mechanical system. This approach enables the finite-time visualization of generalized stable and unstable manifolds, attractors and generalized KAM curves under arbitrary forcing, when Poincaré maps are not available. We illustrate these results by detailed visualizations of the key finite-time invariant sets of conservatively and dissipatively forced Duffing oscillators.

A. Hadjighasem
Department of Mechanical Engineering, McGill University, 817 Sherbrooke Ave. West, Montreal, Quebec H3A 2K6, Canada
e-mail: alireza.hadjighasem@mail.mcgill.ca

M. Farazmand · G. Haller (✉)
Institute for Mechanical Systems, ETH Zürich, Tannenstrasse 3, 8092 Zürich, Switzerland
e-mail: georgehaller@ethz.ch

M. Farazmand
Department of Mathematics, ETH Zürich, Rämistrasse 101, 8092 Zürich, Switzerland
e-mail: farazmand@imes.mavt.ethz.ch

**Keywords** Stability of mechanical systems · Non-autonomous dynamical systems · Invariant manifolds · Coherent structures

## 1 Introduction

A number of numerical and analytical techniques are available to analyze externally forced nonlinear mechanical systems. Indeed, perturbation methods, Lyapunov exponents, Poincaré maps, phase space embeddings and other tools have been become broadly used in mechanics [1, 2]. Still, most of these techniques, are only applicable to nonlinear systems subject to autonomous (time-independent), time-periodic, or time-quasiperiodic forcing.

These recurrent types of forcing allow for the analysis of asymptotic features based on a finite-time sample of the underlying flow map—the mapping that takes initial conditions to their later states. Indeed, to understand the phase space dynamics of an autonomous system, knowing the flow map over an arbitrary short (but finite) time interval is enough, as all trends can be reproduced by the repeated applications of this short-time map. Similarly, the period map of a time-periodic system (or a one-parameter family of flow maps for a time-quasiperiodic system) renders asymptotic conclusions about recurrent features, such as periodic and quasiperiodic orbits, their stable and unstable manifolds, attractors, etc.

By contrast, the identification of key features in the response of a nonlinear system under time-aperiodic forcing has remained an open problem. Mathematically, the lack of precise temporal recurrence in such systems prevents the use of a compact extended phase space on which the forced system would be autonomous. This lack of compactness, in turn, renders most techniques of nonlinear dynamics inapplicable. Even more importantly, a finite-time understanding of the flow map can no longer be used to gain a full understanding of a (potentially ever-changing) non-autonomous system.

Why would one want to develop an understanding of mechanical systems under aperiodic, finite-time forcing conditions? The most important reason is that most realistic forms of forcing will take time to build up, and hence will be transient in nature, at least initially. Even if the forcing is time-independent, the finite-time transient response of a mechanical system is often crucial to its design, as the largest stresses and strains invariably occur during this period.

Similar challenges arise in fluid dynamics, where temporally aperiodic unsteady flows are the rule rather than the exception. Observational or numerical data for such fluid flows are only available for a limited time interval, and some key features of the flow may only be present for an even shorter time. For instance, the conditions creating a hurricane in the atmosphere are transient, rather than periodic, in nature, and the hurricane itself will generally only exist for less than two weeks [3]. As a result, available asymptotic methods are clearly inapplicable to its study, even though there is great interest in uncovering its internal structure and overall dynamics.

In response to these challenges in fluid dynamics, a number of diagnostic tools have been developed [4, 5]. Only very recently, however, has a rigorous mathematical theory emerged for dynamical structures in finite-time aperiodic flow data [6]. This theory finds that finite-time invariant structures in a dynamical system are governed by intrinsic, metric properties of the finite-time flow map. Specifically, in two-dimensional unsteady flows, structures acting as transport barriers can be uncovered with the help of geodesics of the Cauchy–Green strain tensor used in continuum mechanics [7]. This approach generalizes and extends earlier work on hyperbolic Lagrangian Coherent Structures (LCS), which are locally most repelling or attracting material lines in the flow [8–11].

In this paper, we review the geodesic transport theory developed in [6] in the context of one-degree-of-freedom, aperiodically forced mechanical systems. We then show how this theory uncovers key invariant sets under both conservative and dissipative forcing in cases where classic techniques, such as Poincaré maps, are not available. Remarkably, these finite-time invariant sets can be explicitly identified as parametrized curves, as opposed to plots requiring post-processing or feature extraction.

The organization of this paper is as follows. Section 2 is divided into two subsections: Sect. 2.1 provides the necessary background for the geodesic theory of transport barriers developed in [6]. In Sect. 2.2, we describe a numerical implementation of this theory that detects finite-time invariant sets as transport barrier. Section 3 presents results from the application of this numerical algorithm to one degree-of-freedom mechanical systems. First, as a proof of concept, Sect. 3.1 considers conservative and dissipative time-periodic Duffing oscillators, comparing their geodesically extracted invariant sets with those obtained form Poincaré maps. Next, Sect. 3.2 deals with invariant sets in aperiodically forced Duffing oscillators, for which Poincaré maps or other rigorous extraction methods are not available. We conclude the paper with a summary and outlook.

## 2 Set-up

The key invariant sets of autonomous and time-periodic dynamical systems–such as fixed points, periodic and quasiperiodic motions, their stable and unstable manifolds, and attractors–are typically distinguished by their asymptotic properties. In contrast, invariant sets in finite-time, aperiodic dynamical systems solely distinguish themselves by their observed impact on trajectory patterns over the finite time interval of their definition. This observed impact is a pronounced lack of trajectory exchange (or transport) across the invariant set, which remains coherent in time, i.e., only undergoes minor deformation. Well-understood, classic examples of such transport barriers include local stable manifolds of saddles, parallel shear jets, and KAM tori of time-periodic conservative systems. Until recently, a common dynamical feature of these barriers has not been identified, hindering the unified detection of transport barriers in general non-autonomous dynamical systems.

As noted recently in [6], however, a common feature of all canonical transport barriers in two dimensions is that they stretch less under the flow than neighboring curves of initial conditions do. This observation leads to a nonstandard calculus of variations problem with unknown endpoints and a singular Lagrangian. Below we recall the solution of this problem from [6], with a notation and terminology adapted to one-degree-of-freedom mechanical oscillators.

A one-degree-of-freedom forced nonlinear oscillator can generally be written as a two-dimensional dynamical system

$$\dot{x} = v(x,t), \qquad x \in U \subset \mathbb{R}^2, \qquad t \in [t_0, t_1], \tag{1}$$

with $U$ denoting an open set in the state space, where the vector $x$ labels tuples of positions and velocities. The vector $v(x,t)$, assumed twice continuously differentiable, contains the velocity and acceleration of the system at state $x$ and at time $t$.

Let $x(t_1; t_0, x_0)$ denote the final state of system (1) at time $t_1$, given its state $x_0$ at an initial time $t_0$. The flow map associated with (1) over this time interval is defined as

$$F_{t_0}^{t_1} : x_0 \longmapsto x(t_1; t_0, x_0), \tag{2}$$

which maps initial states to final states at $t_1$. The Cauchy–Green (CG) strain tensor associated with the flow map (2) is defined as

$$C_{t_0}^{t_1}(x_0) = \left[DF_{t_0}^{t_1}(x_0)\right]^\top DF_{t_0}^{t_1}(x_0), \tag{3}$$

where $DF_{t_0}^{t_1}$ denotes the gradient of the flow map (2), and the symbol $\top$ refers to matrix transposition.

Note that the CG tensor is symmetric and positive definite. As a result, it has two positive eigenvalues $0 < \lambda_1 \leq \lambda_2$ and an orthonormal eigenbasis $\{\xi_1, \xi_2\}$. We fix this eigenbasis so that

$$\begin{aligned} &C_{t_0}^{t_1}(x_0)\xi_i(x_0) = \lambda_i(x_0)\xi_i(x_0), \\ &\left|\xi_i(x_0)\right| = 1, \ i \in \{1,2\}, \\ &\xi_2(x_0) = \Omega\xi_1(x_0), \quad \Omega = \begin{pmatrix} 0 & -1 \\ 1 & 0 \end{pmatrix}. \end{aligned} \tag{4}$$

We suppress the dependence of $\lambda_i$ and $\xi_i$ on $t_0$ and $t_1$ for notational simplicity.

### 2.1 Geodesic transport barriers in phase space

A *material line* $\gamma_t = F_{t_0}^t(\gamma_{t_0})$ is an evolving curve of initial conditions $\gamma_{t_0}$ under the flow map $F_{t_0}^t$. As shown in [6], for such a material line to be a locally least-stretching curve over $[t_0, t_1]$, it must be a hyperbolic, a parabolic or an elliptic line (see Fig. 1).

The initial position $\gamma_{t_0}$ of a hyperbolic material line is tangent to the vector field $\xi_1$ at all its points. Such material lines are compressed by the flow by locally the largest rate, while repelling all nearby material lines at an exponential-in-time rate. The classic example of a hyperbolic material lines is the unstable manifold of a saddle-type fixed point.

A parabolic material line is an open material curve whose initial position $\gamma_{t_0}$ is tangent to one of the directions of locally largest shear. At each point of the phase space, the two directions of locally largest shear are given by

$$\eta_\pm = \sqrt{\frac{\sqrt{\lambda_2}}{\sqrt{\lambda_1}+\sqrt{\lambda_2}}}\xi_1 \pm \sqrt{\frac{\sqrt{\lambda_1}}{\sqrt{\lambda_1}+\sqrt{\lambda_2}}}\xi_2, \tag{5}$$

as derived in [6]. Parabolic material lines still repel most nearby material lines (except for those parallel to them), but only at a rate that is linear in time. Classic examples of parabolic material lines in fluid mechanics are the parallel trajectories of a steady shear flow.

Finally, an elliptic material line is a closed curve whose initial position $\gamma_{t_0}$ is tangent to one of the two directions of locally largest shear given in (5). As a result, elliptic lines also repel nearby, nonparallel material lines at a linear rate, but they also enclose a connected region. Classic examples of elliptic material lines are closed trajectories of a steady, circular shear flow, such as a vortex.

Initial positions of hyperbolic material lines are, by definition, *strainlines*, i.e., trajectories of the autonomous differential equation

$$r' = \xi_1(r), \quad r \in U \subset \mathbb{R}^2, \tag{6}$$

where $r : [0, \ell] \mapsto U$ is the parametrization of the strainline by arclength. A *hyperbolic barrier* is then a strainline that is locally the closest to least-stretching geodesics of the CG tensor, with the latter viewed as a metric tensor on the domain $U$ of the phase space. The pointwise closeness of strainlines to least-stretching geodesics can be computed in terms of the invariants of the CG strain tensor. Specifically, the $C^2$ distance

**Fig. 1** The three types of transport barrier in two-dimensional flows (Color figure online)

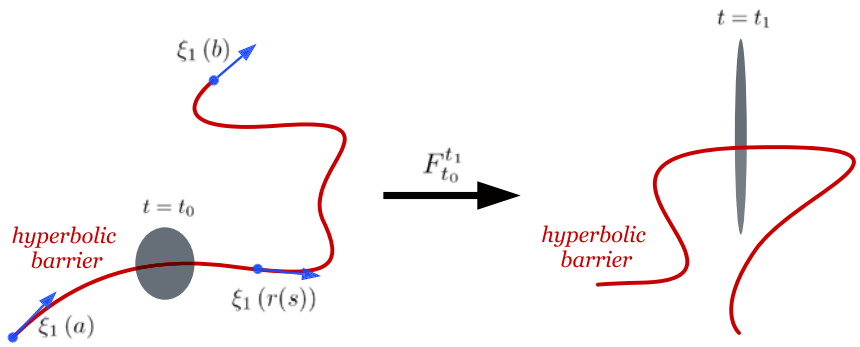


(a) A repelling hyperbolic barrier (red curve) repels nearby trajectories (gray blob) exponentially fast in time.

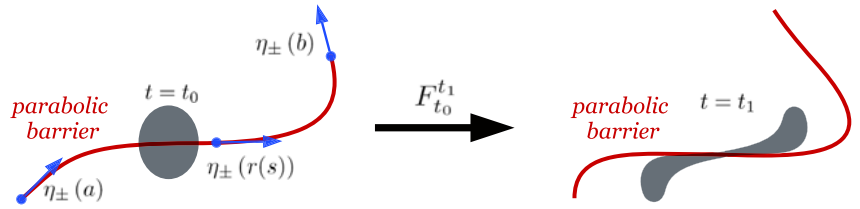


(b) A parabolic barrier (red curve) is an open curve that has the locally largest rate of Lagrangian shear along its tangent.

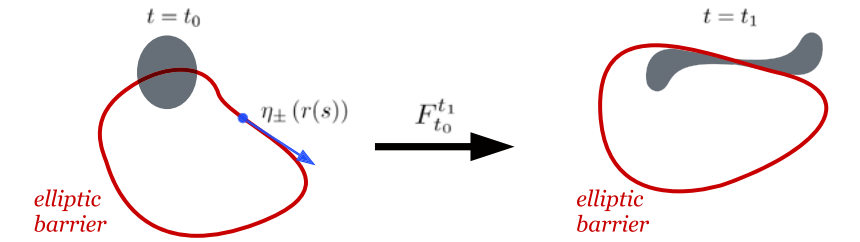


(c) An elliptic barrier (red curve) is a *closed* curve with the same dynamical property as a paraolic barrier.

(difference of tangents plus difference of curvatures) of a strainline from the least-stretching geodesic of $C_{t_0}^t$ through a point $x_0$ is given by the *geodesic strain deviation*

$$d_g^{\xi_1}(x_0) = \frac{|\langle \nabla\lambda_2, \xi_2\rangle + 2\lambda_2\kappa_1|}{2\lambda_2^3}, \tag{7}$$

with $\kappa_1(x_0)$ denoting the curvature of the strainline through $x_0$ [6]. A hyperbolic barrier is a compact strainline segment on which $d_g^{\xi_1}$ is pointwise below a small threshold value, and whose averaged $d_g^{\xi_1}$ value is locally minimal relative to all neighboring strainlines.

Similarly, initial positions of parabolic and elliptic material lines are, by definition, *shearlines*, i.e., trajectories of the autonomous differential equation

$$r' = \eta_\pm(r), \quad r \in U \subset \mathbb{R}^2. \tag{8}$$

A *parabolic barrier* is an open shearline that is close to least-stretching geodesics of the CG tensor. The pointwise $C^2$-closeness of shearlines to least-stretching geodesics is given by the *geodesic shear deviation*

$$d_g^{\eta_\pm}(x_0) = \frac{\sqrt{1+\lambda_2} - \sqrt{\lambda_1}}{\sqrt{1+\lambda_2}} + \left| \frac{\langle \nabla\lambda_2, \xi_1\rangle}{2\lambda_2\sqrt{1+\lambda_2}} \mp \frac{\langle \nabla\lambda_2, \xi_2\rangle(\sqrt{1+\lambda_2}^3 - \sqrt{\lambda_2}^5)}{2\lambda_2^3\sqrt{1+\lambda_2}^3} \right|$$

$$\mp \frac{\kappa_1[\sqrt{\lambda_2}^5 + (1-\lambda_2^2)\sqrt{1+\lambda_2}]}{\lambda_2^2\sqrt{1+\lambda_2}} + \frac{\kappa_2}{\sqrt{1+\lambda_2}}, \tag{9}$$

with $\kappa_2(x_0)$ denoting the curvature of the $\xi_2$ vector field at the point $x_0$ [6]. The geodesic shear deviation should pointwise be below a small threshold level for an open shearline to qualify as a parabolic barrier. Similarly, a closed shearline is an *elliptic barrier* if its pointwise geodesic shear deviation is smaller than small threshold level.

For the purposes of the present discussion, we call a mechanical system of the form (1) *conservative* if it has vanishing divergence, i.e., $\nabla \cdot v(x,t) = 0$, with $\nabla$ referring to differentiation with respect to $x$. This property implies that flow map of (1) conserves phase-space area for all times [13].

While a typical material line in such a conservative system will still stretch and deform significantly over time, the length of a shearline will always be preserved under the area-preserving flow map $F_{t_0}^{t_1}$ (cf. [6]). An elliptic barrier in a conservative system will, therefore, have the same enclosed area and arclength at the initial time $t_0$ and at the final time $t_1$. These two conservation properties imply that an elliptic barrier in a non-autonomous conservative system may only undergo translation, rotation and some slight deformation, but will otherwise preserve its overall shape. As a result, the interior of an elliptic barrier will not mix with the rest of the phase-space, making elliptic barriers the ideal generalized KAM curves in aperiodically forced conservative mechanical systems.

### 2.2 Computation of invariant sets as transport barriers

In this section, we describe numerical algorithms for the extraction of hyperbolic and elliptic barriers in a one-degree-of-freedom mechanical system with general time dependence. Parabolic barriers can in principle also exist in mechanical systems, but they do not arise in the simple examples we study below. In contrast, parabolic barriers are more common in geophysical fluid mechanics where they typically represent unsteady shear jets.

Our numerical algorithms require a careful computation of the CG tensor. In most mechanical systems, trajectories separate rapidly, resulting in an exponential growth in the entries of the CG tensor. This growth necessitates the use of a well-resolved grid, as well as the deployment of high-end integrators in solving for the trajectories of (1) starting form this grid. Further computational challenges arise from the handling of the unavoidable orientational discontinuities and isolated singularities of the eigenvector fields $\xi_1$ and $\xi_2$. The reader is referred to Farazmand & Haller [10] for a detailed treatment of these computational aspects.

As a zeroth step, we fix a sufficiently dense grid $\mathcal{G}_0$ of initial conditions in the phase-space $U$, then advect the grid points from time $t_0$ to time $t_1$ under system (1). This gives a numerical representation of the flow map $F_{t_0}^{t_1}$ over the grid $\mathcal{G}_0$. The CG tensor field $C_{t_0}^{t_1}$ is then obtained by definition (3) from $F_{t_0}^{t_1}$. In computing the gradient $DF_{t_0}^{t_1}$, we use careful finite differencing over an auxiliary grid, as described in [10].

Since, at each point $x_0 \in \mathcal{G}_0$, the tensor $C_{t_0}^{t_1}(x_0)$ is a two-by-two matrix, computing its eigenvalues $\{\lambda_1, \lambda_2\}$ and eigenvectors $\{\xi_1, \xi_2\}$ is straightforward. With the CG eigenvalues and eigenvectors at hand, we locate the hyperbolic barriers using the following algorithm.

**Algorithm 1** (Locating hyperbolic barriers)

1. Fix a small positive parameter $\epsilon_{\xi_1}$ as the admissible upper bound for the pointwise geodesic strain deviation of hyperbolic transport barriers.
2. Calculate strainlines by solving the ODE (6) numerically, with linear interpolation of the strain vector field between grid points. Truncate strainlines to compact segments whose pointwise geodesic strain deviation is below $\epsilon_{\xi_1}$.
3. Locate hyperbolic barriers as strainline segments $\gamma_{t_0}$ with locally minimal relative stretching, i.e., strainline segments that locally minimize the function

$$q(\gamma_{t_0}) = \frac{l(\gamma_{t_1})}{l(\gamma_{t_0})}. \tag{10}$$

Here $l(\gamma_{t_0})$ and $l(\gamma_{t_1})$ denote the length of the strainline $\gamma_{t_0}$ and the length of its advected image $\gamma_{t_1}$, respectively.

Computing the relative stretching (10) of a strainline $\gamma_{t_0}$, in principle, requires advecting the strainline to time $t_1$. However, as shown in [6], the length of the advected image satisfies $l(\gamma_{t_1}) = \int_{\gamma_{t_0}} \sqrt{\lambda_1}\, ds$, where the

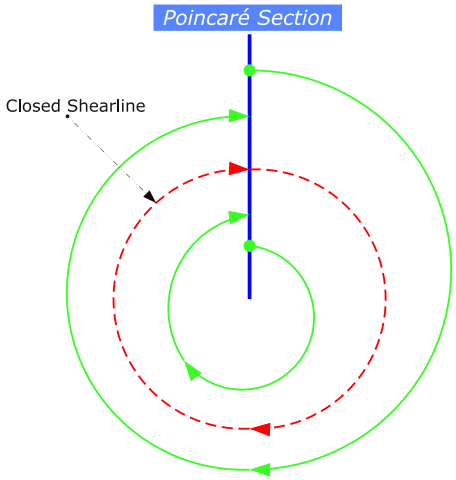


**Fig. 2** Locating closed shearlines using a Poincaré section of the shear vector field. Closed shearlines pass through the fixed points of the corresponding Poincaré map

integration is carried out along the strainline $\gamma_{t_0}$. This renders the strainline advection unnecessary.

Numerical experiments have shown that a direct computation of $\xi_1$ is usually less accurate than that of $\xi_2$ due to the attracting nature of strongest eigenvector of the CG tensor [10]. For this reason, computing $\xi_1$ as an orthogonal rotation of $\xi_2$ is preferable. Moreover, it has been shown [12] that strainlines can be computed more accurately as advected images of *stretchlines*, i.e. curves that are everywhere tangent to the second eigenvector of the *backward-time* CG tensor $C_{t_1}^{t_0}$. In the present paper, this approach is taken for computing the strainlines.

Computing elliptic barriers amounts to finding limit cycles of the ODE (8). To this end, we follow the approach used in [6, 12] by first identifying candidate regions for shear limit cycles visually, then calculating the Poincaré map on a one-dimensional section transverse to the flow within the candidate region (see Fig. 2). Hyperbolic fixed points of this map can be located by iteration, marking limit cycles of the shear vector field (see [12] for more detail).

This process is used in the following algorithm to locate elliptic barriers.

**Algorithm 2** (Locating elliptic barriers)

1. Fix a small positive parameter $\varepsilon_{\eta_\pm}$ as the admissible upper bound for the average geodesic shear deviation of elliptic transport barriers.
2. Visually locate the regions where closed shearlines may exist. Construct a sufficiently dense Poincaré map, as discussed above. Locate the fixed points of the Poincaré map by iteration.
3. Compute the full closed shearlines emanating from the fixed points of the Poincaré map.
4. Locate elliptic barriers as closed shearlines whose average geodesic deviation $\langle d_g^{\eta_\pm} \rangle$ satisfies $\langle d_g^{\eta_\pm} \rangle < \epsilon_{\eta_\pm}$.

In the next section, we use the above algorithms for locating invariant sets in simple forced and damped nonlinear oscillators.

## 3 Results

We demonstrate the implementation of the geodesic theory of transport barriers on four Duffing-type oscillators. As a proof of concept, in the first two examples (Sect. 3.1), we consider *periodically* forced Duffing oscillators for which we can explicitly verify our results using an appropriately defined Poincaré map.

The next two examples deal with *aperiodically* forced Duffing oscillators (Sect. 3.2). In these examples, despite the absence of a Poincaré map, we still obtain the key invariant sets as hyperbolic and elliptic barriers.

To implement Algorithms 1 and 2 in the forthcoming examples, the CG tensor is computed over a uniform grid $\mathcal{G}_0$ of $1000 \times 1000$ points. A fourth order Runge–Kutta method with variable step-size (ODE45 in MATLAB) is used to solve the first-order ODEs (1), (6), and (8) numerically. The absolute and relative tolerances of the ODE solver are set equal to $10^{-4}$ and $10^{-6}$, respectively. Off the grid points, the strain and shear vector fields are obtained by bilinear interpolation.

In each case, the Poincaré map of Algorithm 2 is approximated by 500 points along the Poincaré section. The zeros of the map are located by a standard secant method.

### 3.1 Proof of concept: periodically forced Duffing oscillator

*Case 1:* Pure periodic forcing, no damping Consider the periodically forced Duffing oscillator

$$\dot{x}_1 = x_2,$$

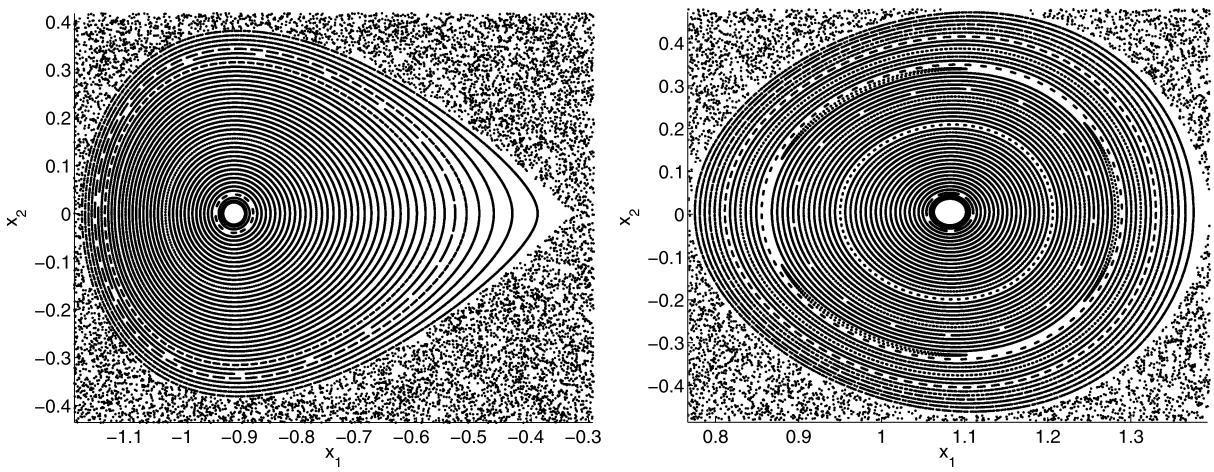


**Fig. 3** Five hundred iterations of the Poincaré map for the periodically forced Duffing oscillator. Two elliptic regions of the phase-space filled by KAM tori are shown

$$\dot{x}_2 = x_1 - x_1^3 + \epsilon\cos(t).$$

For $\epsilon = 0$, the system is integrable with one hyperbolic fixed point at $(0, 0)$, and two elliptic fixed points $(1, 0)$ and $(-1, 0)$, respectively. As is well known, there are two homoclinic orbits connected to the hyperbolic fixed point, each enclosing an elliptic fixed point, which is in turn surrounded by periodic orbits. These periodic orbits appear as closed invariant curves for the Poincaré map $P := F_0^{2\pi}$. The fixed points of the flow are also fixed points of $P$.

For $0 < \epsilon \ll 1$, the Kolmogorov–Arnold–Moser (KAM) theory [13] guarantees the survival of most closed invariant sets for $P$. Figure 3 shows these surviving invariant sets (KAM curves) of $P$ obtained for $\epsilon = 0.08$. For the KAM curves to appear continuous-looking, nearly 500 iterations of $P$ were needed, requiring the advection of initial conditions up to time $t = 1000\pi$. The stochastic region surrounding the KAM curves is due to chaotic dynamics arising from the transverse intersections of the stable and unstable manifold of the perturbed hyperbolic fixed point of $P$.

The surviving KAM curves are well-known, classic examples of transport barriers. We would like to capture as many of them as possible as elliptic barriers using the geodesic transport theory described in previous sections. Note that not all KAM curves are expected to prevail as locally least-stretching curves for a given choice of the observational time interval $[t_0, t_1]$; some of these curves may take longer to prevail due to their shape and shearing properties.

We use the elliptic barrier extraction algorithm of Sect. 2.2 with $\varepsilon_{\eta_\pm} = 0.7$. Figure 4 shows the resulting shearlines in the KAM regions, with the closed ones marked by red. Note that these shearlines were obtained from the CG tensor computed over the time interval $[0, 8\pi]$, spanning just four iterations of the Poincaré map. Despite this low number of iterations, the highlighted elliptic barriers are practically indistinguishable form the KAM curves obtained from 500 iterations.

Figure 5 shows the convergence of an elliptic barrier to a KAM curve as the integration time $T = t_1 - t_0$ increases. Note how the average geodesic deviation $\langle d_g^{\eta_\pm} \rangle$ decreases with increasing $T$, indicating decreasing deviation from nearby Cauchy–Green geodesics.

Remarkably, constructing these elliptic barriers requires significantly shorter integration time (only four forcing periods) in comparison to visualization through the Poincaré map, which required 500 forcing periods to reveal KAM curves as continuous objects. Clearly, the overall computational cost for constructing elliptic barriers still comes out to be higher, since the CG tensor needs to be constructed on a relatively dense grid $\mathcal{G}_0$, as discussed in Sect. 2.2. This high computational cost will be justified, however, in the case of aperiodic forcing (Sect. 3.2), where no Poincaré map is available.

In the context of one-degree-of-freedom mechanical systems, the outermost elliptic barrier marks the boundary between regions of chaotic dynamics and regions of oscillations that are regular on a macroscopic

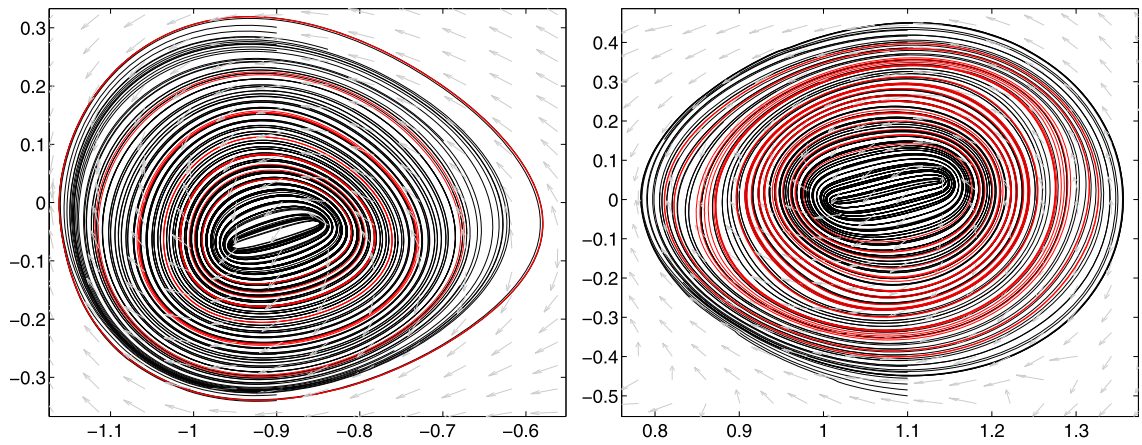

**Fig. 4** Shearlines (*black*) of the periodically forced Duffing oscillator computed at $t_0 = 0$, with integration time $T = 8\pi$. The extracted elliptic barriers with $\langle d_g^{\eta\pm} \rangle \leq \varepsilon_{\eta\pm} = 0.7$ are shown in *red* (Color figure online)

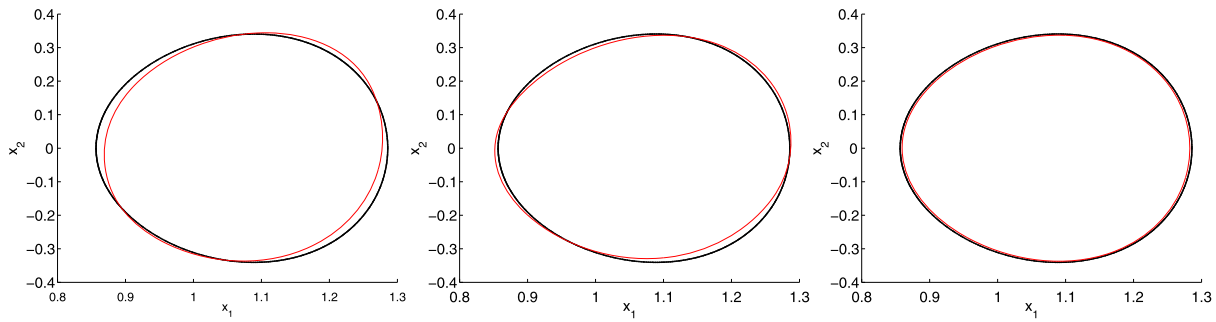

(a) $T = 8\pi$, $\langle d_g^{\eta\pm} \rangle = 0.5991$. (b) $T = 10\pi$, $\langle d_g^{\eta\pm} \rangle = 0.3889$. (c) $T = 12\pi$, $\langle d_g^{\eta\pm} \rangle = 0.2355$.

**Fig. 5** Convergence of an elliptic barrier (*red*) to a KAM curve (*black*) as the integration time $T = t_1 - t_0$ increases. The gradually decreasing average geodesic deviation $\langle d_g^{\eta\pm} \rangle$ confirms the convergence to Cauchy–Green geodesics that closely shadow the underlying KAM torus (Color figure online)

scale. To demonstrate this sharp dividing property of elliptic barriers, we show the evolution of system (12) from three initial states, two of which are inside the elliptic region and one of which is outside (Fig. 6a). The system exhibits rapid changes in its state when started from outside the elliptic region. In contrast, more regular behavior is observed for trajectories starting inside the elliptic region. This behavior is further depicted in Fig. 7, which shows the evolution of the $x_1$-coordinate of the trajectories as a function of time.

*Case 2:* Periodic forcing and damping Consider now the damped-forced Duffing oscillator

$$\dot{x}_1 = x_2,$$
$$\dot{x}_2 = x_1 - x_1^3 - \delta x_2 + \epsilon \cos(t), \tag{11}$$

with $\delta = 0.15$ and $\epsilon = 0.3$. This system is known to have a chaotic attractor that appears as an invariant set of the Poincaré map $P = F_0^{2\pi}$ (see, e.g., [1]). Here, we show that the attractor can be very closely approximated by hyperbolic barriers computed via Algorithm 1.

Figure 8a shows strainlines computed backward in time with $t_0 = 0$ and integration time $T = t_1 - t_0 = -8\pi$. The strainline with globally minimal relative stretching (10) is shown in Fig. 8b. Black dots mark the points where the geodesic deviation $d_g^{\xi_1}$ exceeds the admissible upper bound $\epsilon_{\xi_1} = 10^{-3}$. At its tail (covered by black dots), the strainline persistently deviates from CG geodesics, and hence should be trun-

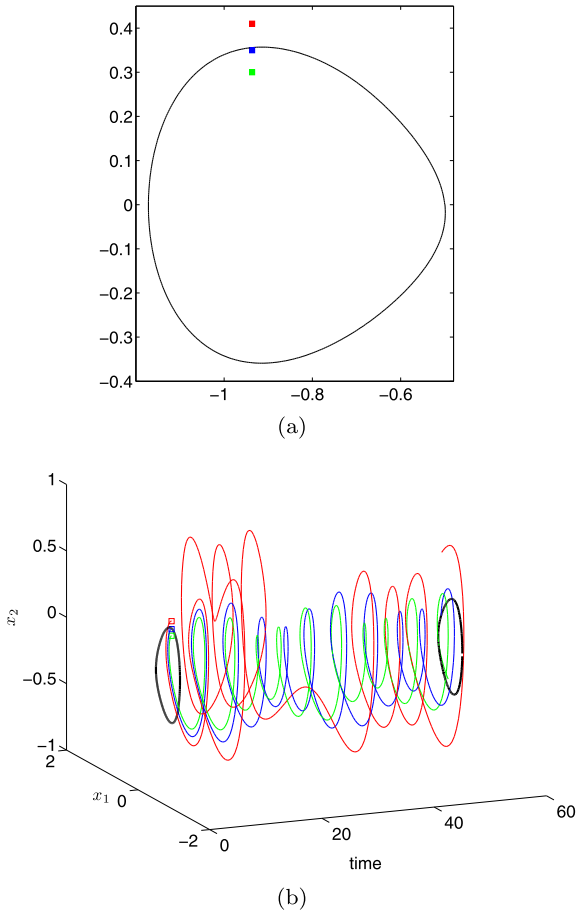


**Fig. 6** (**a**) The outermost elliptic barrier (*black curve*) and three initial conditions: Two inside the elliptic barrier (*blue* and *green*) and one outside the elliptic barrier (*red*). (**b**) The corresponding trajectories are shown in the extended phase space of $(x_1, x_2, t)$. The *closed black curves* mark the elliptic barrier at $t_0 = 0$ and $t_1 = 16\pi$ (Color figure online)

cated. The resulting hyperbolic barrier, as a finite-time approximation to the chaotic attractor, is shown in Fig. 8c.

The approximate location of the attractor can also be revealed by applying the Poincaré map to a few initial conditions (tracers) released from the basin of attraction. For long enough advection time, the initial conditions converge to the attractor highlighting its position (see Figs. 9a and 9b). In Fig. 9c, the hyperbolic barrier is superimposed on the advected tracers showing close agreement between the two. Figure 9d shows the tracers advected for a longer time ($T = 40\pi$) together with the hyperbolic barrier; the two virtually coincide. Note that the hyperbolic barrier is a smooth, parametrized curve (computed as a trajectory of (6)), while the tracers form a set of scattered points.

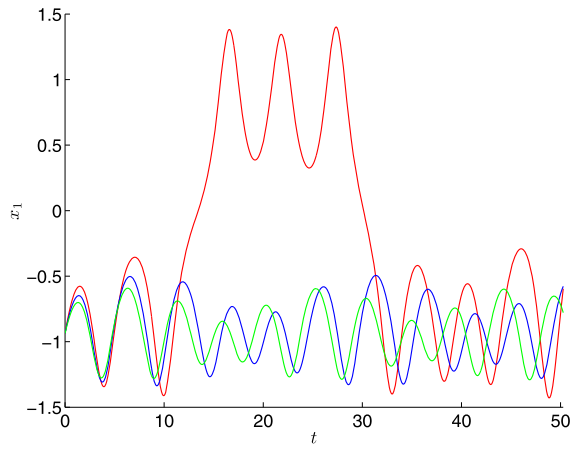


**Fig. 7** The $x_1$-coordinate of the trajectories of Fig. 6

### 3.2 The aperiodically forced Duffing oscillator

In the next two examples, we study aperiodically forced Duffing oscillators. In the presence of aperiodic forcing, the Poincaré map $P$ is no longer defined as the system lacks any recurrent behavior. However, KAM-type curves (i.e., closed curves, resisting significant deformation) and generalized stable and unstable manifolds (i.e., most repelling and attracting material lines) exist in the phase-space and determine the overall dynamics of the system.

*Case 1:* Purely aperiodic forcing, no damping Consider the Duffing oscillator

$$\begin{aligned} \dot{x}_1 &= x_2, \\ \dot{x}_2 &= x_1 - x_1^3 + f(t), \end{aligned} \tag{12}$$

where $f(t)$ is an aperiodic forcing function obtained from a chaotic one-dimensional map (see Fig. 10).

While KAM theory is no longer applicable, one may still expect KAM-type barriers to survive for small forcing amplitudes. Such barriers would no longer be repeating themselves periodically in the extended phase space. Instead, a generalized KAM barrier is expected to be an invariant cylinder, with cross sections showing only minor deformation. The exis-

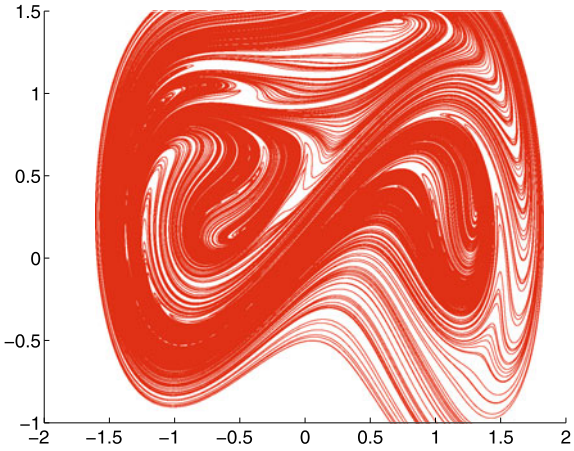

(a) Strainlines computed for the damped-forced Duffing oscillator (11) at time $t_0 = 0$, with the integration time $T = -8\pi$.

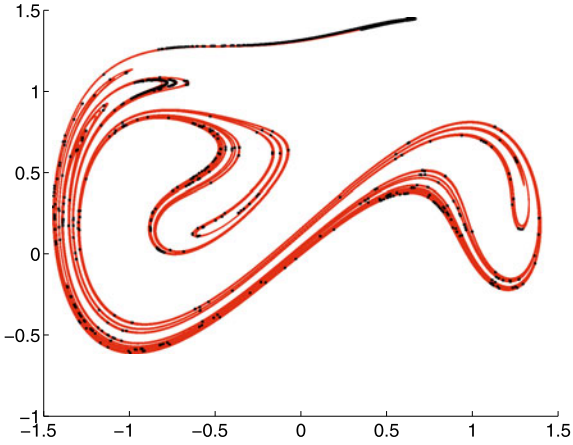

(b) The strainline (red) with globally minimum relative stretching. Points with $d_g^{\xi_1} > 10^{-3}$ are highlighted as black dots.

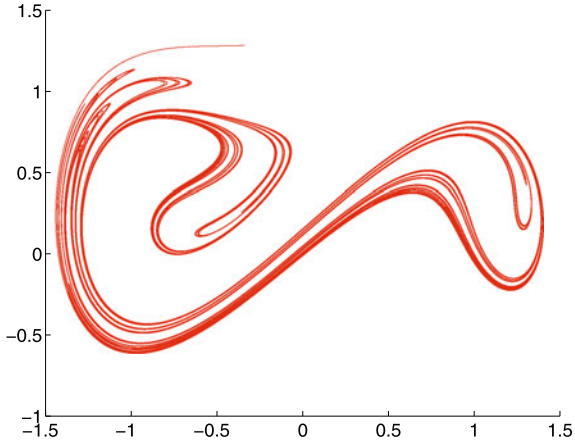

(c) Final approximation of the chaotic attractor by a single, continuous strainline with minimal geodesic deviation.

**Fig. 8** Construction of the attractor of the damped-forced Duffing oscillator as a hyperbolic transport barrier (Color figure online)

tence of such structures can, however, be no longer studied via Poincaré maps.

Figure 11 confirms that generalized KAM-type curves, obtained as elliptic barriers, do exist in this problem. These barriers are computed over the time interval $[0, 4\pi]$ (i.e. $t_0 = 0$ and $t_1 = t_0 + T = 4\pi$). As discussed in Sect. 2.1, the arclength of an elliptic barrier at the initial time $t_0$ is equal to the arclength of its advected image under the flow map $F_{t_0}^{t_1}$ at the final time $t_1$. This arclength preservation is illustrated numerically in Fig. 12, which shows the relative stretching,

$$\delta\ell(t) = \frac{\ell(\gamma_t) - \ell(\gamma_0)}{\ell(\gamma_0)} \tag{13}$$

of the time-$t$ image $\gamma_t$ of an elliptic barrier $\gamma_0$, with $\ell$ referring to the arclength of the curve. Ideally, the relative stretching of each elliptic barrier should be zero at time $t_1 = 4\pi$, i.e. $\delta\ell(4\pi) = 0$. Instead, we find that the relative stretching $\delta\ell(4\pi)$ of the computed elliptic barriers is at most 1.5 %. This deviation from zero arises from numerical errors in the computation of the

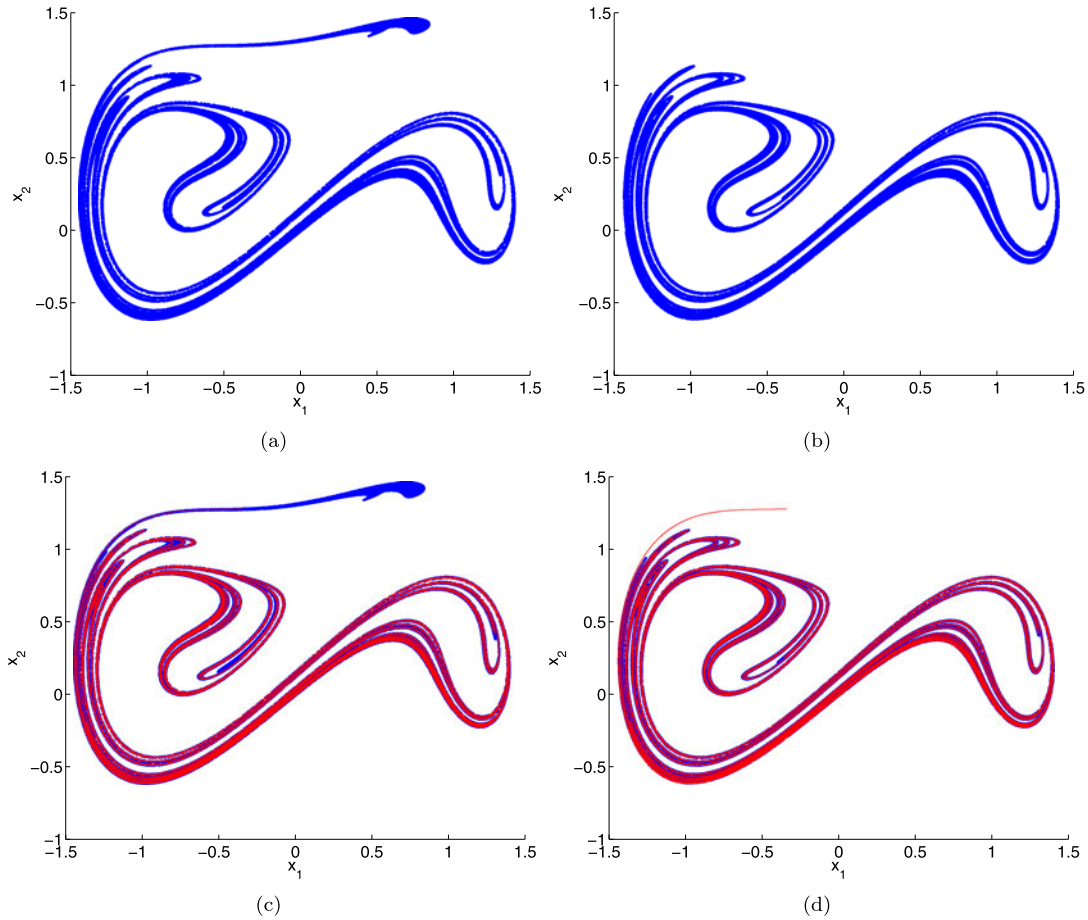


**Fig. 9** (**a**) Attractor of system (11) obtained from four iterates of the Poincaré map. (**b**) Attractor obtained from 20 iterates of the Poincaré map. (**c**) Attractor computed as a hyperbolic barrier (*red*), compared with the Poincaré map (*blue*) computed for the same integration time (four iterates). (**d**) Comparison of attractor computed as a hyperbolic barrier (*red*) with the one obtained from 20 iteration of the Poincaré map (*blue*). The integration time for locating the hyperbolic barrier is $T = t_1 - t_0 = -8\pi$ (Color figure online)

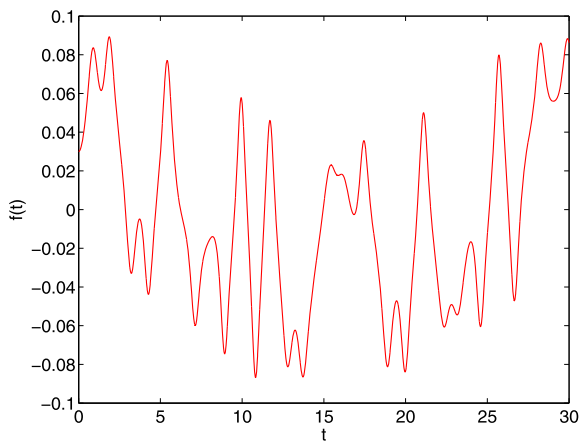


**Fig. 10** Chaotic forcing function $f(t)$ for (12)

CG strain tensor $C_{t_0}^{t_1}$, which in turn causes small inaccuracies in the computation of closed shearlines.

As noted earlier, the small relative stretching and the conservation of enclosed area for an elliptic barrier in incompressible flow only allows for small deformations when the barrier is advected in time. This is illustrated in Fig. 13, which shows the blue elliptic barrier of Fig. 11b in the extended phase-space. Each constant-time slice of the figure is the advected image of the barrier.

Finally, we point out that the stability of the trajectories inside elliptic barriers show a similar trend as in the case of the periodically forced Duffing equation (Figs. 6 and 7). Namely, perturbations inside the ellip-

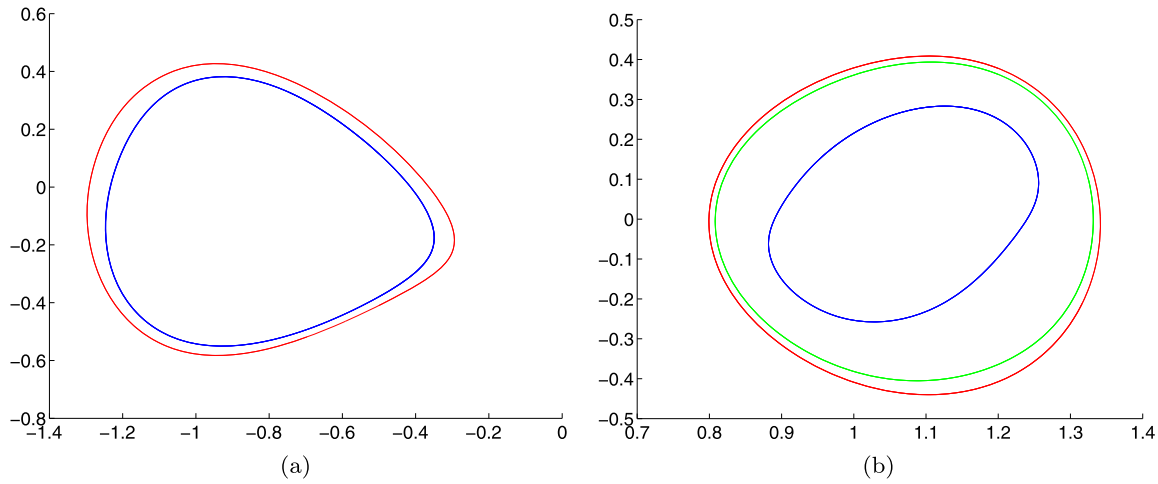


**Fig. 11** Closed shearlines for (12) computed in two elliptic regions. The figure shows the shearlines at time $t_0 = 0$. The integration time is $T = 4\pi$

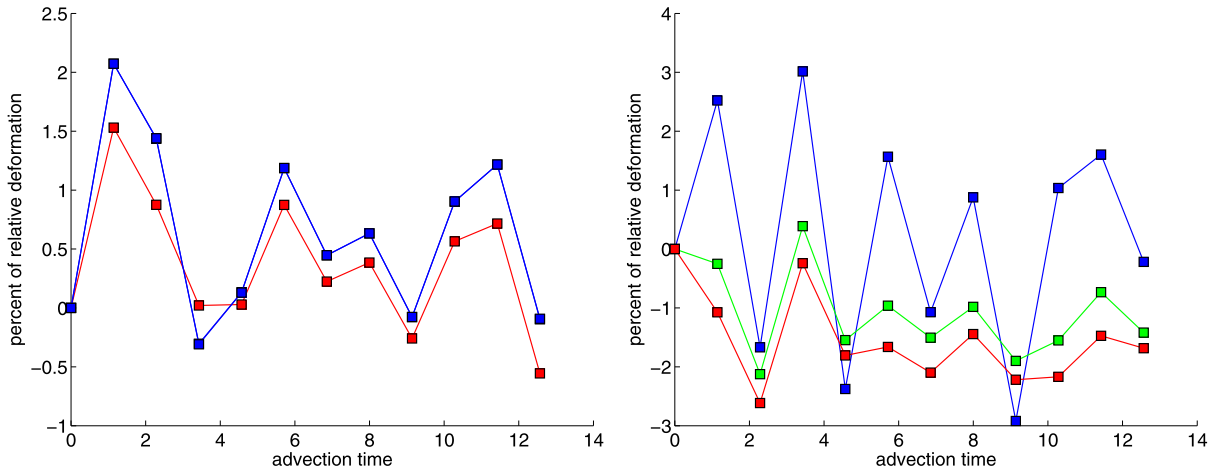


**Fig. 12** The relative stretching $\delta\ell(t) \times 100$ of closed shearlines of Fig. 11. The colors correspond to those of Fig. 11. By their arclength preservation property, the advected elliptic barriers must theoretically have the same arclength at times $t_0 = 0$ and $t_1 = 4\pi$. The numerical error in arclength conservation is small overall, but more noticeable for oscillations with large amplitudes (*green* and *red curves* of the *right panel*) (Color figure online)

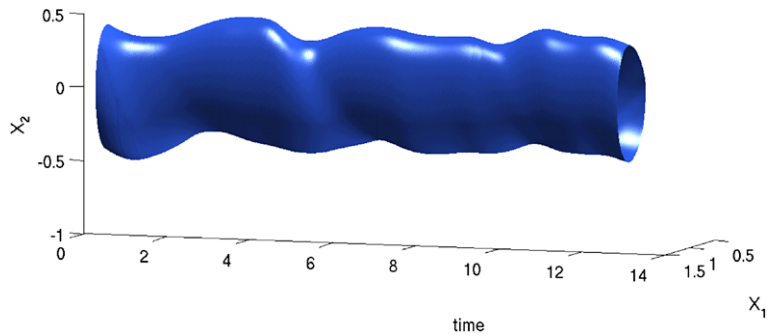


**Fig. 13** Generalized KAM-type cylinder in the extended phase space of the aperiodically forced undamped Duffing oscillator. The cylinder is obtained by advection of the closed shearline shown in blue in Fig. 11(b)

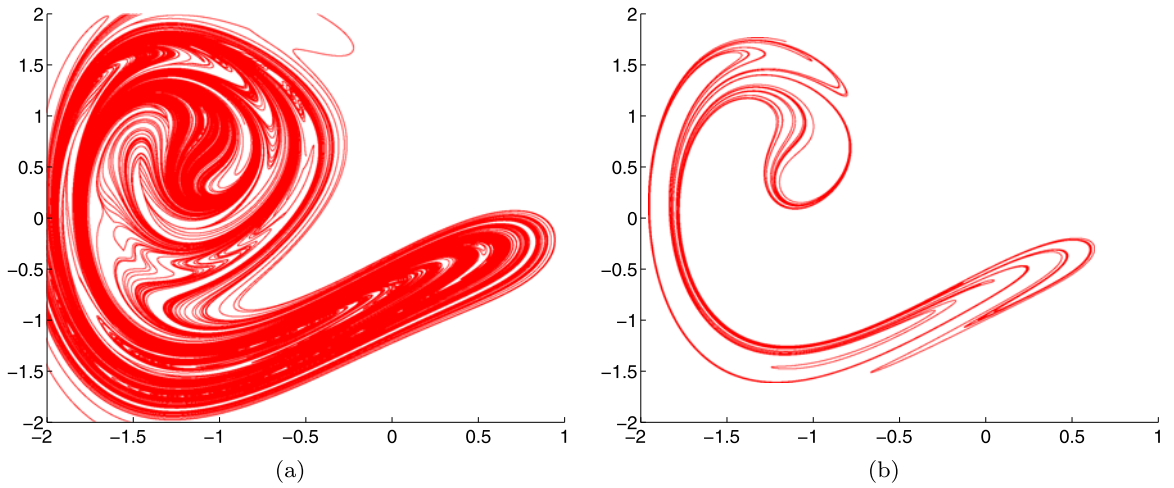


**Fig. 14** (**a**) Strainlines computed in backward time from $t_0 = 30$ to $t_1 = 10$. (**b**) The resulting hyperbolic barrier extracted with maximum admissible geodesic deviation of $\epsilon_{\xi_1} = 10^{-5}$

tic regions remain small while they grow significantly inside the hyperbolic regions.

*Case 2:* Aperiodic forcing with damping In this final example, we consider the aperiodically forced, damped Duffing oscillator

$$\begin{aligned} \dot{x}_1 &= x_2, \\ \dot{x}_2 &= x_1 - x_1^3 - \delta x_2 + f(t), \end{aligned} \tag{14}$$

with damping coefficient $\delta = 0.15$. The forcing function $f(t)$ is similar to that of Case I above, but with an amplitude twice as large. As a result, none of the elliptic barriers survive even in the absence of damping.

Again, because of the aperiodic forcing, the behavior of this system is a priori unknown and cannot be explored using Poincaré maps. In order to investigate the existence of an attractor, strainlines (Fig. 14a) are computed from the backward-time CG strain tensor $C_{t_0}^{t_1}$ with $t_0 = 30$ and $t_1 = 10$. The strainline with minimum relative stretching (10) is then extracted. The part of this strainline satisfying $d_g^{\xi_1} < \epsilon_{\xi_1}$ is considered as the most influential hyperbolic barrier (Fig. 14b). The admissible upper bound $\epsilon_{\xi_1}$ for the geodesic deviation is fixed as $10^{-5}$.

In order to confirm the existence of the extracted attractor, we advect tracer particles in forward time, first from time $t_1 = 10$ to time $t_0 = 30$, then from $t_1 = 0$ to time $t_0 = 30$. Because of the fast-varying dynamics and weak dissipation, a relatively long advection time is required for the tracers to converge to the attractor. Figure 15 shows the evolution of tracers over $[t_1, t_0]$. Note that the attractor inferred from the tracers is less well pronounced than the hyperbolic barrier extracted over the same length of time. This shows a clear advantage for geodesic transport theory over simple numerical experiments with tracer advection. For a longer integration time from $t_0 = 0$ to $t = 30$, the tracers eventually converge to the hyperbolic barrier.

Repelling hyperbolic barriers can be computed similarly using forward-time computations. Figure 16 shows both hyperbolic barriers (stable and unstable manifolds) at time $t_0 = 30$. The repelling barrier is computed from the CG strain tensor $\mathbf{C}_{t_0}^{t_1}$ with $t_0 = 30$ and $t_1 = 50$.

## 4 Summary and conclusions

We have shown how the recently developed geodesic theory of transport barriers [6] in fluid flows can be adapted to compute finite-time invariant sets in one-degree-of-freedom mechanical systems with general forcing. Specifically, in the presence of general time dependence, temporally aperiodic stable- and unstable manifolds, attractors, as well as generalized KAM tori can be located as hyperbolic and elliptic barriers, respectively. The hyperbolic barriers are computed as distinguished *strainlines*, i.e. material lines along

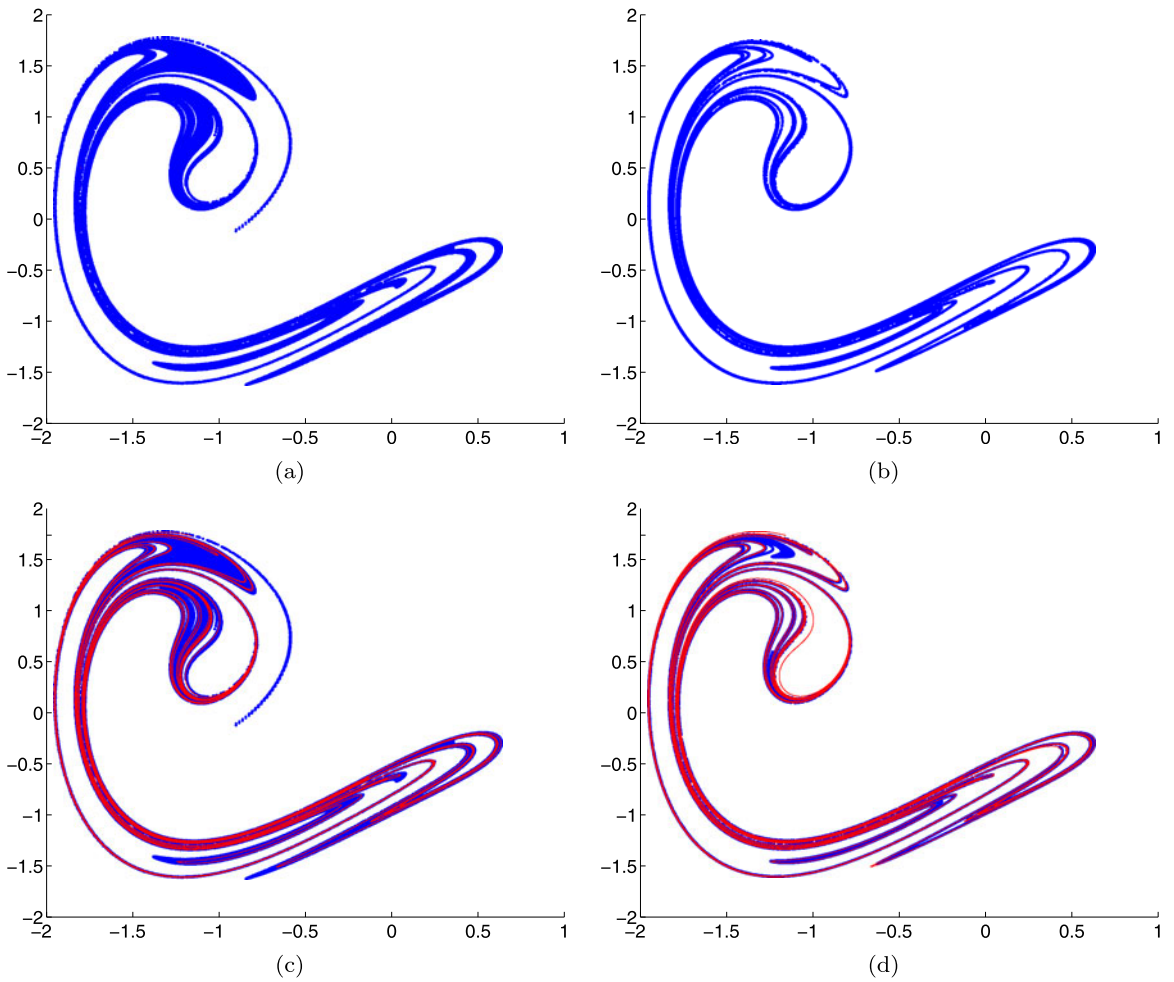


**Fig. 15** (**a**) Tracers advected over the time interval from $t_1 = 10$ to $t_0 = 30$. (**b**) Tracers advected over a longer time interval from $t_1 = 0$ to $t_0 = 30$. (**c**) The hyperbolic barrier (*red*) superimposed on the tracers advected for the same time interval. (**d**) Comparison of the hyperbolic barrier (*red*) with the tracers advected for the longer time interval (Color figure online)

which the Lagrangian strain is locally maximized. The elliptic barriers, on the other hand, appear as distinguished *shearlines*, i.e. material lines along which the Lagrangian shear is locally maximized. The barriers are finally identified as strainlines and shearlines that are most closely approximated by least-stretching geodesics of the metric induced by Cauchy–Green strain tensor.

We have used four simple examples for illustration. First, as benchmarks, we considered periodically forced Duffing equations for which stable and unstable manifolds, attractors and KAM curves can also be obtained as invariant sets of an appropriately defined Poincaré map. We have shown that elliptic barriers, computed as closed shearlines, coincide with the KAM curves. Also, stable and unstable manifolds, as well as attractors, can be recovered as hyperbolic barriers. More precisely, as the integration time $T = t_1 - t_0$ of the Cauchy–Green strain tensor $\mathbf{C}_{t_0}^{t_1}$ increases, the elliptic barriers in the periodically forced Duffing equations converge to KAM curves. Similarly, the chaotic attractor of the periodically forced and damped Duffing equation is more and more closely delineated by a hyperbolic barrier computed from the backward-time Cauchy–Green strain tensor $\mathbf{C}_{t_1}^{t_0}$ for increasing $T = t_0 - t_1$ where $t_0 > t_1$.

In the second set of examples, we have computed similar structures for an aperiodically forced Duff-

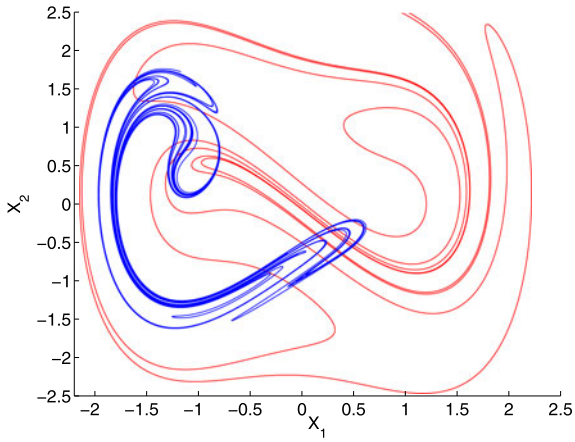


**Fig. 16** Attracting (*blue*) and repelling (*red*) barriers at $t_0 = 30$ extracted from backward-time and forward-time computations, respectively (Color figure online)

ing oscillator with and without damping. In this case, Poincaré maps are no longer well-defined for the system, and hence we had to advect tracer particles to verify the predictions of the geodesic theory. Notably, tracer advection takes longer time to reveal the structures in full detail than the geodesic theory does. Also, tracer advection is only affective as a visualization tool if it relies on a small number of particles, which in turn assumes that one already roughly knows the location of the invariant set to be visualized. Finally, unlike scattered tracer points, geodesic barriers are recovered as parametrized smooth curves that provide a solid foundation for further analysis or highly accurate advection.

In our examples, elliptic barriers have shown themselves as borders of subsets of the phase-space that barely deform over time. In fact, as illustrated in Fig. 6, outermost elliptic barriers define the boundary between chaotic and regular dynamics. Trajectories initiated inside elliptic barriers remain confined and robust with respect to small perturbations. We believe that this property could be exploited for stabilizing mechanical systems with general time dependence. For instance, formulating an optimal control problem for generating elliptic behavior in a desired part of the phase-space is a possible approach.

Undoubtedly, the efficient and accurate computation of invariant sets as geodesic transport barriers requires dedicated computational resources. Smart algorithms reducing the computational cost are clearly of interest. Parallel programming (both at CPU and GPU levels) has previously been employed for Lagrangian coherent structure calculations and should be useful in the present setting as well (see e.g. [14]). Other adaptive techniques are also available to lower the numerical cost by reducing the computations to regions of interest (see e.g. [15, 16]).

In principle, invariant sets in higher-degree-of-freedom mechanical systems could also be captured by similar techniques as locally least-stretching surfaces. The development of the underlying multi-dimensional theory and computational platform, however, is still under way.

**Acknowledgements** M.F. would like to thank the Department of Mathematics at McGill University where this research was partially carried out. G.H. acknowledges partial support by the Canadian NSERC under grant 401839-11.

## References

1. Guckenheimer, J., Holmes, P.: Nonlinear Oscillations, Dynamical Systems, and Bifurcations of Vector Fields. Springer, Berlin (1990)
2. Strogatz, S.H.: Nonlinear Dynamics and Chaos. Westview Press, Boulder (2008)
3. Rutherford, B., Dangelmayr, G.: A three-dimensional Lagrangian hurricane eyewall computation. Q. J. R. Meteorol. Soc. **136**, 1931–1944 (2010)
4. Peacock, T., Dabiri, J.: Introduction to Focus Issue: Lagrangian Coherent Structures. Chaos **20**(1) (2010)
5. Lai, Y.C., Tél, T.: Transient Chaos: Complex Dynamics on Finite Time Scales. Springer, Berlin (2011)
6. Haller, G., Beron-Vera, F.J.: Geodesic theory of transport barriers in two-dimensional flows. Physica D **241**(20), 1680–1702 (2012)
7. Truesdell, C., Noll, W., Antman, S.: The Non-linear Field Theories of Mechanics, vol. 3. Springer, Berlin (2004)
8. Haller, G.: A variational theory of hyperbolic Lagrangian coherent structures. Physica D **240**(7), 574–598 (2011)
9. Farazmand, M., Haller, G.: Erratum and addendum to "A variational theory of hyperbolic Lagrangian coherent structures (vol. 240, p. 574, 2011).". Physica D **241**(4), 439–441 (2012)
10. Farazmand, M., Haller, G.: Computing Lagrangian coherent structures from their variational theory. Chaos **22**(1), 013128 (2012)
11. Haller, G., Yuan, G.: Lagrangian coherent structures and mixing in two-dimensional turbulence. Physica D **147**(3–4), 352–370 (2000)
12. Farazmand, M., Haller, G.: Geodesic transport barriers in two-dimensional turbulence. J. Fluid Mech. (2012). (preprint)
13. Arnold, V.I.: Mathematical Methods of Classical Mechanics. Springer, Berlin (1989)

14. Garth, C., Li, C.S., Tricoche, X., Hansen, C.D., Hageni, H.: Visualization of coherent structures in transient 2D flows. In: Hege, H.C., Polthier, K., Scheuermann, G. (eds.) Topology-Based Methods in Visualization. II. Mathematics and Visualization, pp. 1–13 (2009)
15. Barakat, S., Garth, C., Tricoche, X.: Interactive computation and rendering of finite-time Lyapunov exponent fields. IEEE Trans. Vis. Comput. Graph. **18**(8), 1368–1380 (2012)
16. Lipinski, D., Cardwell, B., Mohseni, K.: A Lagrangian analysis of a two-dimensional airfoil with vortex shedding. J. Phys. A, Math. Theor. **41**(34), 344011 (2008)